Heliyon 9 (2023) e17358

Contents lists available at ScienceDirect

Heliyon

journal homepage: www.cell.com/heliyon

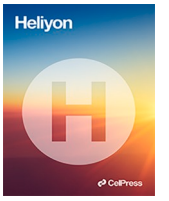

# Structural, Hirshfeld surface and molecular docking studies of a new organotin(IV)-phosphoric triamide complex and an amidophosphoric acid ester proposed as possible SARS-CoV-2 and Monkeypox inhibitors

Maedeh Khorram [a], Atekeh Tarahhomi [a,*], Arie van der Lee [b], Grégory Excoffier [c]

[a] *Department of Chemistry, Semnan University, Semnan 35131-19111, Iran*
[b] *IEM, Université de Montpellier, CNRS, ENSCM, Montpellier, France*
[c] *Aix Marseille Univ, CNRS, Centrale Marseille, FSCM, Spectropole, Marseille, France*

A R T I C L E I N F O

*Keywords:*
Organotin(IV)-phosphoramide complex
X-ray crystallography
Hirshfeld surface analysis
Molecular docking
SARS-CoV-2
Monkeypox

A B S T R A C T

Phosphoramides and their complexes are attractive compounds due to their significant inhibiting functionality in biological medicine. In this paper, a novel organotin(IV)-phosphoramide complex ($Sn(CH_3)_2Cl_2\{[(3\text{-}Cl)C_6H_4NH]P(O)[NC_4H_8O]_2\}_2$, **1**), derived from a reaction between phosphoric triamide ligand with dimethyltin dichloride, and a new amidophosphoric acid ester ($[OCH_2C(CH_3)_2CH_2O]P(O)[N(CH_3)CH_2C_6H_5]$, **2**), prepared from the condensation of a cyclic chlorophosphate reagent with *N*-methylbenzylamine, are structurally characterized and *in silico* investigated as potential SARS-CoV-2 and Monkeypox inhibitors by molecular docking simulation. Both compounds crystallize in the monoclinic crystal system with space group $P2_1/c$. The asymmetric unit of the complex **1** consists of one-half molecule, where $Sn^{IV}$ is located on an inversion center, while the asymmetric part of **2** consists of one whole molecule. In the complex **1**, the tin atom adopts a six-coordinate octahedral geometry with *trans* groups of $(Cl)_2$, $(CH_3)_2$ and $(PO)_2$ (PO = phosphoric triamide ligand). The molecular architecture consists of the N–H···Cl hydrogen bonds stretching as a 1D linear arrangement along the *b* axis with intermediate $R_2^2(12)$ ring motifs, whereas in the case of **2**, the crystal packing is devoid of any classical hydrogen bond interaction. Furthermore, a graphical analysis by using Hirshfeld surface method identifies the most important intermolecular interactions being of the type H···Cl/Cl···H (for **1**) and H···O/O···H (for **1** and **2**), covering the hydrogen bond interactions N–H···Cl and C–H···O=P, respectively, which turn out to be favoured. A biological molecular docking simulation on the studied compounds provides evidence to suggest a significant inhibitory potential against SARS-COV-2 (6LU7) and Monkeypox (4QWO) especially for 6LU7 with a binding energy around −6 kcal/mol competing with current effective drugs against this virus (with a binding energy around −5 and −7 kcal/mol). It is worth noting that this report is the first case of an inhibitory potential evaluation of phosphoramide compounds on Monkeypox.

* Corresponding author.
*E-mail address:* tarahhomi.at@semnan.ac.ir (A. Tarahhomi).

https://doi.org/10.1016/j.heliyon.2023.e17358
Received 30 March 2023; Received in revised form 13 June 2023; Accepted 14 June 2023
Available online 19 June 2023

## Synopsis

The crystalline forms of two new phosphoramide compounds, a novel organotin(IV)-phosphoric triamide complex and a new amidophosphoric acid ester, are investigated by using single-crystal X-ray diffraction and spectral study completed with the Hirshfeld surface and molecular docking analyses. A significant inhibitory potential against SARS-CoV-2 and Monkeypox, especially for the former case, is suggested for the studied compounds by helping the biological docking simulation.


## 1. Introduction

The coronavirus disease of 2019 (COVID-19) pandemic caused by the Severe Acute Respiratory Syndrome Coronavirus 2 (SARS-CoV-2) and Monkeypox of the family Poxviridae are two challenging illnesses becoming a significant worldwide problem since around 2019. During this crisis, many investigations have been carried out to find potential inhibiting drugs against these viruses such as Remdesivir, Tenofovir, Sofosbuvir, chloroquine and hydroxychloroquine for coronavirus [1,2], and Tecovirimat and Brincidofovir for Monkeypox [3]. However, no approved and decisive medications are known until now to treat these viruses [4,5] which motivates researchers to explore new molecular families as effective drugs against these viruses to treat their consequences on human health.

A number of phosphoramide compounds and their organotin(IV) complexes have been structurally studied [6–8], where some of

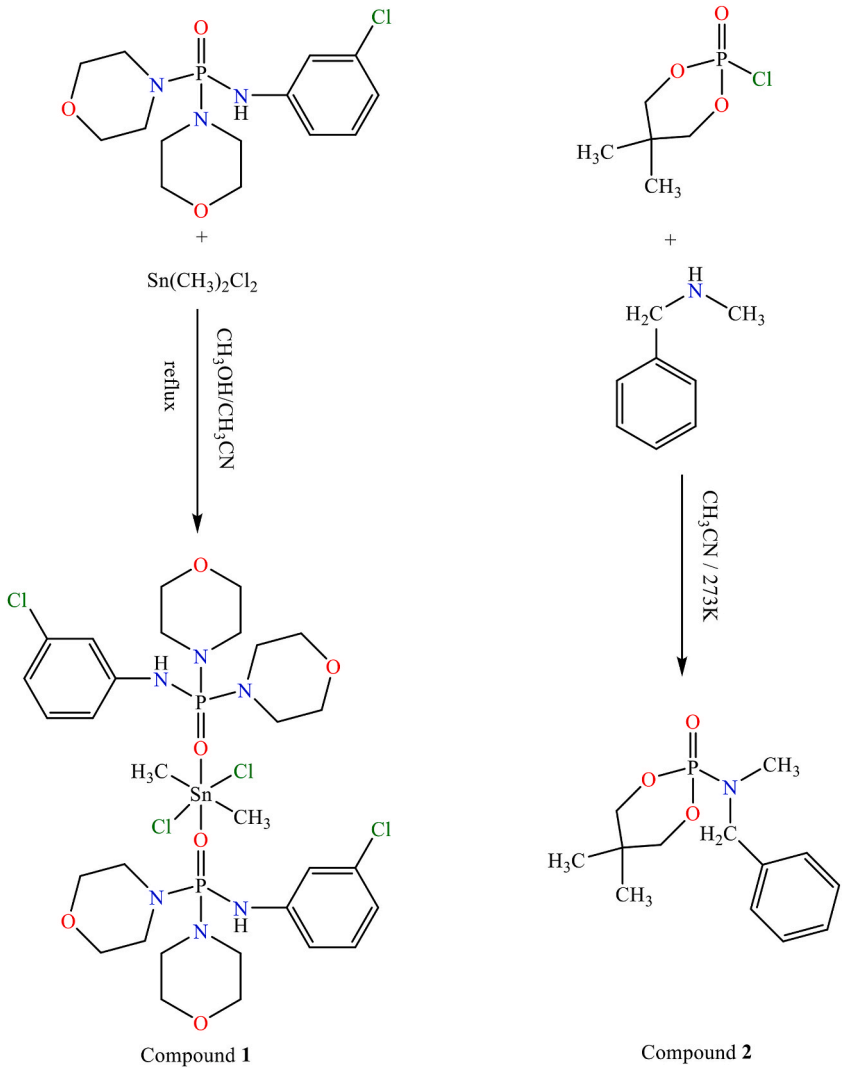


**Scheme 1.** Chemical structures of compounds **1** and **2**.

them have significant medicine applications such as antiviral, antitumor and anticancer activities [9–12]. Antibacterial and antimicrobial properties also have been found for some of phosphoramidate derivatives [13–16]. Moreover, some of these compounds are found to be the significant promising candidates to inhibit coronavirus [17–19]: some of the current not-optimal anti-coronavirus drugs, Remdesivir and Sofosbuvir, belong to the phosphoramides family [20,21]. However, there are no reports of the inhibitory potential of phosphoramide compounds on Monkeypox.

The development of new drugs by clinical trials is a confident method to test their efficiency, but may take a long time and the use of costly equipment. For this reason computer-aided drug discovery is being widely utilized to evaluate the potential of a compound as a drug to inhibit the disease-causing organisms, and molecular docking simulations in particular accelerates the choice of potential drugs for clinical trials [22–25]. In the case of phosphoramide compounds, some reports suggest them as possible inhibitors against SARS-CoV-2 by molecular docking studies that evaluate the binding interactions between the target protein of coronavirus and the tested drug compound [26–28].

With this background in mind, we select here the molecular structures of two different sub-classes of phosphoramides, a novel organotin(IV)-phosphoric triamide complex, $Sn(CH_3)_2Cl_2\{[(3\text{-}Cl)C_6H_4NH]P(O)[NC_4H_8O]_2\}_2$ (**1**) and a new amidophosphoric acid ester, $[OCH_2C(CH_3)_2CH_2O]P(O)[N(CH_3)CH_2C_6H_5]$ (**2**) (Scheme 1) in order to comparison of their molecular assemblies and biology simulations. First, the synthesis, characterization and the solid-state crystal structures of these two compounds are discussed based on the results of single-crystal X-ray diffraction, IR and NMR spectroscopies. The intermolecular interactions in the new structures are analyzed by 3D Hirshfeld surface maps and 2D fingerprint plots. The inhibitory effect of the compounds **1** and **2** against the coronavirus (Main Protease ($M^{Pro}$) of SARS CoV-2, 6LU7) and Monkeypox (the A42R Profilin-like protein of Monkeypox virus with PDB ID: 4QWO) are investigated by the molecular docking method, where the evaluation of the inhibitory potential of such compounds against Monkeypox is reported for the first time. We hope that such investigation based on the computer-aided drug discovery of docking approach which is here employed as an evaluation plan to consider the possibility of the inhibitory effect of the studied compounds on the biological targets can accelerate the choice of potential drugs based on such compounds for clinical trials in future works.

It is worth noting that in here two new compounds **1** and **2** belonging to two different families of phosphoramides have been selected to investigate their crystal structures and molecular docking simulations as well as to explore their differences and similarities providing new insights into the effect of these differences and similarities on their structural and inhibitory properties. Moreover, in the case of **1**, we reported the crystal structure and molecular docking study of its free ligand ($[(3\text{-}Cl)C_6H_4NH]P(O)[NC_4H_8O]_2$) in our previous literature [28] and in the case of **2**, no complex structure of it has been reported so far (CSD, version 5.42 [29]) as our efforts have not been adequate so far.

## 2. Experimental

### 2.1. Instrumentation

$^1H$, $^{13}C$, $^{31}P\{^1H\}$, $^{119}Sn\{^1H\}$ NMR spectra were recorded on a Bruker Avance III 300 MHz spectrometer. $^1H/^{13}C$, $^{31}P$ and $^{119}Sn$ chemical shifts were defined compared to TMS, 85% $H_3PO_4$ and $Sn(CH_3)_4$, respectively, as external standard. For the IR analysis, the spectra of solid compounds in KBr pellets were recorded in the 4000–400 $cm^{-1}$ range using a Bruker ALPHA FT-IR spectrometer.

### 2.2. Syntheses and crystallization

1) Synthesis of $Sn(CH_3)_2Cl_2\{[(3\text{-}Cl)C_6H_4NH]P(O)[NC_4H_8O]_2\}_2$ (**1**)

For the preparation of this complex, the $[(3\text{-}Cl)C_6H_4NH]P(O)[NC_4H_8O]_2$ phosphoric triamide ligand was first synthesized by the method reported by Najarianzadeh et al. [28]. In the next step, $[(3\text{-}Cl)C_6H_4NH]P(O)[NC_4H_8O]_2$ (1.00 mmol, 0.35 mg) and $Sn(CH_3)_2Cl_2$ (0.50 mmol, 0.11 mg) were dissolved in a mixture of $CH_3OH$ (20 mL) and $CH_3CN$ (10 mL). The mixture was refluxed for 48 h and then the reaction mixture was cooled to room temperature and the solvents were allowed to evaporate. Crystals suitable for single crystal X-ray analysis were obtained by recrystallization of **1** in $CH_3CN/CH(CH_3)_2OH/DMF$ (3:3:1) at room temperature.

**Data for 1: IR (KBr, ῡ, $cm^{-1}$):** 3205 (N–H), 2951, 2860, 1599, 1488, 1452, 1387, 1348, 1300, 1259, 1163 (P═O), 1140, 1132, 1092, 972, 862, 777, 735, 687, 600, 509, 492, 442; **$^1H$ NMR** (300.13 MHz, DMSO-$d_6$, 300.0 K, TMS): δ = 1.01 (s, 6H, $2CH_3$, $^2J(^{119}Sn, H)$ = 54.5 Hz [satellites]), 3.00 (m, 16H, $NC_4H_8O$ ring), 3.46 (m, 16H, $NC_4H_8O$ ring), 6.84–7.22 (m, 4H, Ar–H), 7.45 (d, $^2J(P,H)$ = 9.7 Hz, 1H, NH); **$^{13}C$ NMR** (75.47 MHz, DMSO-$d_6$, 300.0 K, TMS): $\delta$ = 22.53 (s, 2C,Sn–$CH_3$), 44.33 (s, 8C, $NC_4H_8O$ ring), 66.45 (d, $^3J(C,P)$ = 5.7 Hz, 8C, $NC_4H_8O$ ring), 116.25 (d, $^3J(C,P)$ = 6.8 Hz, $2C_{Ar}$), 117.14 (d, $^3J(C,P)$ = 6.6 Hz, $2C_{Ar}$), 119.82 (s, $2C_{Ar}$), 130.39 (s, $2C_{Ar}$), 133.09 (s, $2C_{Ar}$), 144.14 (m, $2C_{Ar}$); **$^{31}P\{^1H\}$ NMR** (121.49 MHz, DMSO, 300.0 K, 85% $H_3PO_4$): δ = 10.30 (s); **$^{119}Sn\{^1H\}$ NMR** (111.86 MHz, $D_2O$, 300.0 K, $Sn(CH_3)_4$): $\delta$ = −107.14 (s). All NMR spectra of **1** can be found in the Supplementary material (Figs. S1–S4).

2) Synthesis of $[OCH_2C(CH_3)_2CH_2O]P(O)[N(CH_3)CH_2C_6H_5]$ (**2**).

To a stirred solution of the starting commercial material $[OCH_2C(CH_3)_2CH_2O]P(O)Cl$ (1.50 mmol, 0.28 mg) in dry acetonitrile (35 mL) a solution of *N*-methylbenzylamine (3.00 mmol, 0.36 mg) at the same solvent was added dropwise at 273 K. After 4 h, the solvent was evaporated at room temperature and the product was washed with distilled water to remove the amine hydrochloride salt. Colorless single crystals were grown by slow evaporation from a solution of **2** in $CH_3OH/CH(CH_3)_2OH/n\text{-}C_6H_{14}$ (3:2:1) at room temperature.

**Data for 2: IR (KBr, ῡ, $cm^{-1}$):** 3063, 2781, 1589, 1464, 1406, 1348, 1244 (P═O), 1223, 1061, 1005, 957 (P–N), 885, 833, 814, 725, 698, 629, 573, 488, 463; **$^{1}$H NMR (300.13 MHz, $CDCl_3$, 300.0 K):** δ = 0.88 (s, 3H, $CH_3$), 1.26 (s, 3H, $CH_3$), 2.61 (d, $^{3}J$(H,P) = 9.7 Hz, 3H, $CH_3$), 3.83 (dd, $^{2}J$(H,H) = 10.8 Hz, $^{3}J$(H,P) = 21.3 Hz, 2H, $CH_{equatorial}$), 4.26 (d, $^{2}J$(H,H) = 10.0 Hz, 2H, $CH_{axial}$), 4.39 (d, $^{2}J$(H,H) = 10.9 Hz, 2H, $CH_2$), 7.26–7.34 (m, 5H, Ar–H); **$^{13}$C NMR (75.47 MHz, $CDCl_3$, 300.0 K):** δ = 20.31 (s, 1C, $CH_3$), 21.93 (s, 1C, $CH_3$), 31.45 (d, $^{2}J$(C,P) = 4.9 Hz, 1C, $CH_3$), 32.50 (d, $^{3}J$(C,P) = 5.1 Hz, 1C, $C(CH_3)_2$), 52.08 (d, $^{3}J$(C,P) = 5.8 Hz, 1C, $CH_2$), 75.89 (d, $^{2}J$(C,P) = 5.6 Hz, 2C, $2CH_2$), 122.00 (s, 1C, Ar), 126.96 (s, 1C, Ar), 127.49 (s, 1C, Ar) 128.05 (s, 1C, Ar), 136.95 (s, 1C, Ar), 137.00 (s, 1C, Ar); **$^{31}$P {$^{1}$H} NMR (121.49 MHz, DMSO-$d_6$, 300.0 K):** δ = 7.51 (s). All NMR spectra of **2** can be found in the Supplementary material (Figs. S5–S7).

### 2.3. Crystal structure determination

Crystal evaluation of **1** and **2** and their X-ray diffraction data collection were conducted with the *CrysAlisPro* software package [30] on an Rigaku Oxford-Diffraction dual Supernova diffractometer equipped with graphite-monochromated Mo-*Kα* (λ = 0.7107 Å; used for **1**) and Cu-*Kα* (λ = 1.5405 Å; used for **2**) X-ray sources. The same package was used for integration of the data using default parameters, correction for Lorentz and polarization effects, and for empirical absorption correction using spherical harmonics employing symmetry-equivalent and redundant data. The structures were solved using the ab initio iterative charge flipping method with parameters described elsewhere [31], with use of the *SUPERFLIP* program [32]. The structures were then refined on $|F|^2$ using full-matrix least-squares procedures as implemented in *CRYSTALS* [33] on all independent reflections with $I > -3\sigma(I)$. Hydrogen atoms were treated as riding on their parent atoms. The *PLATON* [34] and *Mercury* [35] programs were utilized for making the ORTEP and packing diagrams.

A full *MOGUL* [36] analysis of **2** did not show any unusual geometric features, but for **1** an unusual O3–P4–N17 angle was found (112.68° to be compared to 105.253° in 24 similar fragments).

### 2.4. Hirshfeld surface analysis

Recently, investigation of intermolecular interactions by using the Hirshfeld surface analysis as a visual facilitation tool has attracted interest from researchers in various fields [37–39]. Here, this analysis as a powerful protocol to obtain information on non-covalent interactions in crystal packing is employed. The Hirshfeld surface (HS) computations were carried up by using *CrystalExplorer* [40] and the HSs were mapped with the $d_{norm}$ property which is a normalized function of distances from the internal ($d_i$) and external atoms ($d_e$) and also with the shape index [41]. The 2D fingerprint (FP) plots derived from the HS by using the $d_i$ and $d_e$ pairs were computed for each interatomic contact and for overall interactions [42]. Moreover, the enrichment ratio (*E*) was utilized to evaluate the intermolecular contacts calculated by the collected data from HS analysis [43], where the *E* ratio larger than unity defines a "favoured" contact and that lower than unity is attributed to a "disfavoured" contact.

### 2.5. Molecular docking study

The inhibitory effects of **1** and **2** against coronavirus (the target protein 6LU7, Protein Data Bank identifier; Main Protease ($M^{Pro}$) of SARS-CoV-2) and monkeypox (the A42R Profilin-like protein of this virus with PDB ID: 4QWO) were evaluated by the molecular docking method. The docking calculations were performed by using the software of AutoDock 4.2 [44] with AutoGrid 4. To obtain the biological results, the molecular docking simulation was run and the best position of the ligand related to the target protein with the lowest energy was selected. For both the 6LU7 and 4QWO structures, the heteroatoms and water molecules were removed using AutoDock tools and then the H atoms were automatically placed on the protein complexes. For the docking simulation of 6LU7 a grid box with 116 × 104 × 126 Å points and a grid-point spacing of 0.591 Å were used and in the case of 4QWO, a grid box of 120 × 114 × 102 Å points with spacing of 0.375 Å was utilized. Moreover, the Discovery studio software [45] was employed to drawn the 2D ligand maps.

## 3. Results and discussion

### 3.1. Spectroscopic studies

In the IR spectrum of complex **1**, the N–H stretching frequency (3205 $cm^{-1}$) illustrates a blue shift relative to the free ligand (3178 and 3148 $cm^{-1}$ [28]) which is attributed to the involvement of the N–H unit in a weaker N–H···Cl (3.270 (3) Å) hydrogen bond in the complex compared with the N–H···O (2.8030 (5) and 2.8015 (5) Å) hydrogen bond in the free ligand confirmed by the X-ray crystallography results [46]. The P═O stretching frequencies of the complex and free ligand also show a considerable change, where the P═O stretching mode occurs at a lower frequency of 1163 $cm^{-1}$ for the complex **1** related to the frequency of 1196 $cm^{-1}$ for the free ligand. In the case of **2**, the most important stretching modes correspond to the P═O and P–N bonds found at 1244 and 957 $cm^{-1}$, respectively.

In the $^{31}$P NMR spectra, the phosphorus signals appear at 10.30 and 7.51 ppm, for **1** and **2,** respectively. The singlet $^{119}$Sn chemical shift of the complex **1** found at −107.14 ppm is consistent with the shifts in similar six-coordinated tin complexes [6,47]. In the $^{1}$H NMR spectra of **1**, the methyl protons of the $(CH_3)_2SnCl_2$ segment appear as a singlet signal at 1.01 ppm with a observable pair of satellites which could be utilized to evaluate the $^{2}J(^{119}Sn,H)$ coupling constant as 54.5 Hz. Two multiplet signals at 3.00 and 3.46 ppm

are assigned to the $CH_2$ protons of the morpholine rings. The aromatic protons of the 3-chloroaniline substituents appear as multiplet peaks in the range 6.84–7.22 ppm. A doublet signal (with $^2J$(P,H) = 9.7 Hz) at 7.45 ppm is corresponds to two N–H protons. In the $^1$H NMR spectra of **2**, the methyl $CH_3$ protons of the esteric ring appear as two singlet peaks at 0.88 and 1.26 ppm and the methyl $CH_3$ protons of the $CH_3$–N are seen at 2.61 ppm as a doublet with a $^3J$(H,P) coupling constant of 9.7 Hz. The equatorial and axial protons of the $CH_2$ groups of the esteric ring are characterized by a doublet of doublet peak at 3.83 ppm (with $^2J$(H,H) = 10.8 Hz and $^3J$(H,P) = 21.3 Hz) and a doublet peak at 4.26 ppm ($^2J$(H,H) = 10.0 Hz), respectively, as such different splitting patterns for the related signals of $H_{equatorial}$ and $H_{axial}$ protons has been observed for the similar compounds [48]. The doublet signal at 4.39 ppm can be assigned to the $CH_2$ protons of the benzyl substituent with the $^3J$(H,P) coupling constant of 10.9 Hz. The aromatic protons of the benzyl substituent give peaks in the range 7.26–7.34 ppm.

For the $^{13}$C NMR spectra of **1**, the methyl carbon atoms of Sn–$CH_3$ show up as a singlet signal at 22.53 ppm. The $CH_2$ carbon atoms of the morpholine rings are revealed as singlet and doublet (with $^3J$(P,C) = 5.7 Hz) signals at 44.33 and 66.45 ppm, respectively. Three singlet, two doublet ($^3J$(P,C) = 6.8 and 6.6 Hz) and one multiplet signals in the range 116.0 − 144.2 ppm are attributed to the aromatic carbon atoms of the 3-chloroaniline substituents. In the case of **2**, the signals related to the methyl $CH_3$ carbon atoms of the esteric ring appear as two singlet at 20.31 and 21.93 ppm and the $CH_3$–N carbon atom appears as a doublet at 31.45 ppm with $^2J$(C,P) = 4.9 Hz. The signal at 32.50 ppm as a doublet with $^3J$(C,P) = 5.1 Hz is related to the $C(CH_3)_2$ carbon atom of the esteric ring. The doublet signals at 52.08 ppm ($^3J$(C,P) = 5.8 Hz) and 75.89 ppm ($^2J$(C,P) = 5.6 Hz) are assigned to the $CH_2$ carbon atoms of the benzyl group and of the esteric ring, respectively. The aromatic carbon atoms of the benzyl substituent are appeared as six singlet peaks at the range 122 to 137 ppm.

### 3.2. X-ray crystallography investigations

The *ORTEP*-style presentations of the molecular structures of **1** and **2** are given in Figs. 1 and 2. Crystal data, data collection and structure refinement details are presented in Table 1. The selected bond lengths and angles are provided in Table S1. The hydrogen bond interactions geometries for both structures are summarized in Table 3.

Both compounds **1** and **2** crystallize in the monoclinic space group $P2_1/c$. The asymmetric unit of the complex **1** is composed of one-half molecule, where $Sn^{IV}$ is located on an inversion center. In the case of the compound **2**, the asymmetric part consists of one whole molecule. A distorted tetrahedral environment of (O═)P[N]$_3$ for **1** and of (O═)P[O]$_2$[N] for **2** is observed for the phosphorous atom.

In **1**, the coordination geometry around the tin atom is a distorted octahedral with the two phosphoric triamide ligands in the *trans* position with respect to each other. Two chlorine atoms and two methyl groups separately are in a *trans* position (Fig. 1). The cyclo-six-membered rings of morpholine substituents accept a nearly-chair conformation with Cremer and Pople puckering parameters [49] Q = 0.559 (5) Å, θ = 3.0 (4)° and φ = 16 (10)° for the O15/C14/C13/N12/C17/C16 ring and Q = 0.574 (4) Å, θ = 176.6 (4)° and φ = 161 (7)° for the O21/C20/C19/N18/C23/C22 ring. In the phosphoric triamide ligand, the sum of the surrounding angles at the secondary N8 atom of the 3-chloroaniline substituent (∠P–N–C + ∠C–N–H + ∠P–N–H) deviates slightly from zero (1.1°) establishing a mainly $sp^2$ hybridization. For the tertiary N12 and N18 atoms of the morpholine substituents, the sum of ∠P–N–C + ∠P–N–C + ∠C–N–C angles are 356.9 (2)° and 356.82 (19)°, respectively, confirming a near $sp^2$ character and an almost planar configuration of these N atoms. Such

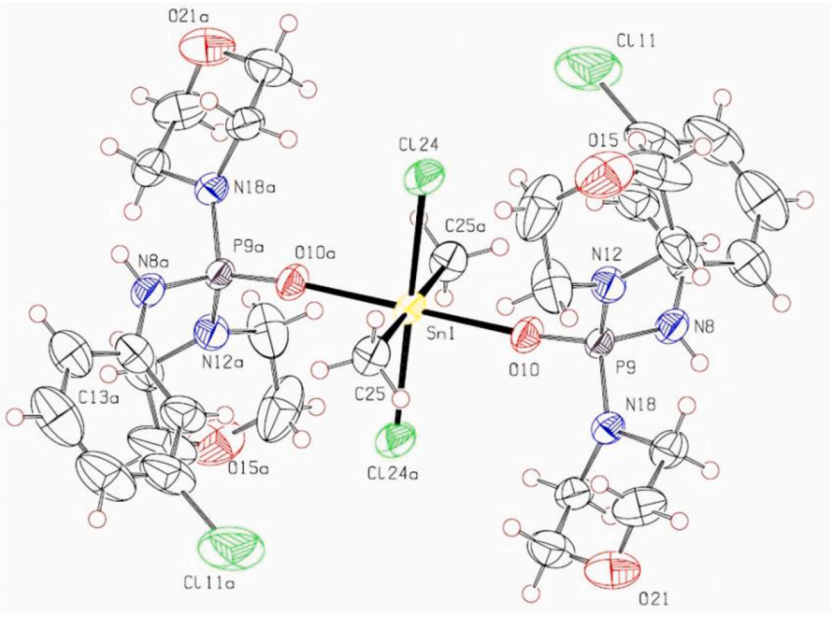


**Fig. 1.** *ORTEP*-style plot and atom-labeling scheme for the structure **1**. Carbon atoms of rings have not been labeled for clarity. Displacement ellipsoids are drawn at the 50% probability level and H atoms are drawn as circles of arbitrary radii.

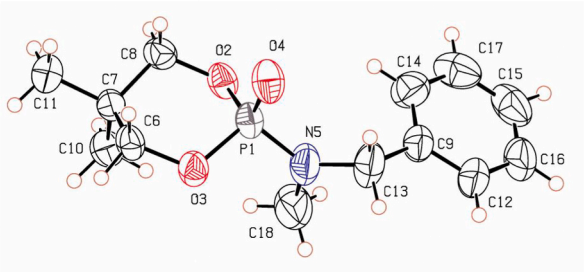


**Fig. 2.** *ORTEP*-style plot and atom-labeling scheme for the structure **2**. Displacement ellipsoids are drawn at the 50% probability level and H atoms are drawn as circles of arbitrary radii.

**Table 1**
Crystal data and structure refinement for the compounds **1** and **2**.

| Compound | 1 | 2 |
|---|---|---|
| Chemical formula | $C_{30}H_{48}Cl_4N_6O_6P_2Sn$ | $C_{13}H_{20}NO_3P$ |
| $M_r$ (gr/mol) | 455.60 | 269.28 |
| Temperature (K) | Monoclinic, $P2_1/c$ | Monoclinic, $P2_1/c$ |
| Crystal system, Space group | 293 | 293 |
| *a, b, c* (Å) | 12.9538 (5), 8.3165 (3), 19.5975 (7) | 13.9865 (3), 8.6469 (1), 13.3191 (3) |
| $\beta$ (°) | 106.564 (4) | 117.137 (2) |
| $V$ (Å$^3$) | 2023.63 (13) | 1433.49 (5) |
| $Z$ | 4 | 4 |
| Radiation type | Mo $K\alpha$ | Cu $K\alpha$ |
| $\mu$ (mm$^{-1}$) | 1.02 | 1.72 |
| $F(000)$ | 932 | 576 |
| Crystal size (mm) | 0.16 × 0.14 × 0.03 | 0.18 × 0.17 × 0.16 |
| Crystal color/habit | Colorless/Plate | Colorless/Prism |
| Diffractometer | Oxford Diffraction SuperNova | Oxford Diffraction SuperNova |
| Theta range for data collection (°) | 2.168 to 33.032 | 2.12 to 28.84 |
| Absorption correction | Multi-scan/*CrysAlis PRO* | Multi-scan/*CrysAlis PRO* |
| $T_{min}$, $T_{max}$ | 0.706, 1.000 | 0.878, 1.000 |
| No. of measured, independent and observed [$I > 2.0\sigma(I)$] reflections | 24796, 6879, 5378 | 16778, 2985, 2684 |
| $R_{int}$ | 0.031 | 0.029 |
| $(\sin\theta/\lambda)_{max}$ (Å$^{-1}$) | 0.767 | 0.629 |
| $R[F^2 > 2\sigma(F^2)]$, $wR(F^2)$, $S$ | 0.040, 0.145, 0.97 | 0.045, 0.134, 0.97 |
| No. of reflections | 6878 | 2985 |
| No. of parameters | 227 | 163 |
| No. of restraints | 4 | 0 |
| H-atom treatment | H atoms treated by a mixture of independent and constrained refinement | H-atom parameters constrained |
| $\Delta\rho_{max}$, $\Delta\rho_{min}$ (e.Å$^{-3}$) | 0.73, −0.76 | 0.23, −0.32 |

**Table 2**
Intermolecular interactions geometries (Å, °) for the compounds **1** and **2**.

| *D*—H···*A* | *D*—H | H···*A* | *D*···*A* | *D*—H···*A* |
|---|---|---|---|---|
| **1** | | | | |
| N8–H8···Cl24$^{i}$ | 0.83 (2) | 2.44 (2) | 3.270 (3) | 173 (3) |
| C20–H202 … π[a] | — | 3.108 | — | 163.90 |
| **2** | | | | |
| C16–H161···O4$^{i}$ | 0.925 | 2.675 | 3.564 (4) | 161.3 |
| C10–H102···O4$^{ii}$ | 0.958 | 2.631 | 3.585 (2) | 173.3 |
| C18–H182 … π[a] | — | 3.574 | — | 137.0 |

Symmetry transformations used to generate equivalent atoms for **1**: (i) $x, y-1, z$; for **2**: (i) $-x+1, y-\frac{1}{2}, -z+\frac{1}{2}$; (ii) $x, -y+\frac{1}{2}, z-\frac{1}{2}$.
[a] For C–H … π interactions $d$(H … $A$) = H … Cg, where Cg = centroid of the phenyl ring.

secondary and tertiary N atoms with a low Lewis-base character cannot be involved in any hydrogen bond interaction as an acceptor. The Sn–O, Sn–Cl and Sn–C bond lengths and the Sn–O–P bond angles (Table S1) are within the expected values [7,50].

For **2**, the P═O, P–O and P–N bond lengths and O═P–N, O═P–O and O–P–N angles are similar to related compounds [27,51]

**Table 3**
Various contacts with their percentage contributions (≥1) along with the surface contacts ($S_X$), the random contacts ($R_{XX}/R_{XY}$) and the extracted enrichment ratios ($E_{XX}/E_{XY}$) for **1** and **2** have been tabulated.

| Contacts | 1 | 2 | | | | | $S_X$ | H | O | C | Cl |
|---|---|---|---|---|---|---|---|---|---|---|---|
| H···H | 55.7 | 67.9 | | | | | **1** | 76.20 | 6.60 | 4.45 | 10.45 |
| H···O/O···H | 13.2 | 19.2 | | | | | **2** | 83.60 | 9.60 | 6.10 | — |
| H···C/C···H | 7.9 | 12.2 | | | | | | | | | |
| H···Cl/Cl···H | 19.9 | — | | | | | | | | | |
| C···Cl/Cl···C | 1.0 | — | | | | | | | | | |
| Atoms | | H | O | C | Cl | | | H | O | C | Cl |
| **1** | $R_{xx}/R_{xy}$ | | | | | **1** | $E_{xx}/E_{xy}$ | | | | |
| H | | 58.06 | 10.06 | 6.78 | 15.93 | H | | 0.96 | 1.31 | 1.17 | 1.25 |
| O | | 10.06 | — | — | | O | | 1.31 | — | — | — |
| C | | 6.78 | — | | 0.93 | C | | 1.17 | — | — | 1.07 |
| Cl | | 15.93 | — | 0.93 | | Cl | | 1.25 | — | 1.07 | — |
| **2** | $R_{xx}/R_{xy}$ | | | | | **2** | $E_{xx}/E_{xy}$ | | | | |
| H | | 69.89 | 16.05 | 10.20 | — | H | | 0.97 | 1.20 | 1.20 | — |
| O | | 16.05 | — | — | — | O | | 1.20 | — | — | — |
| C | | 10.20 | — | — | — | C | | 1.20 | — | — | — |

(Table S1). The tertiary amine N5 of this compound has a $sp^2$ hybridization and a planar configuration reflected in the sum of the surrounding angles (∠P–N–C + ∠P–N–C + ∠C–N–C) about 360° (360.0 (16)°). Moreover, in this tertiary N atom, the C–N–C angle (115.96 (18)°) is significantly smaller than the two related P–N–C angles (121.61 (15)° and 122.43 (15)°) [52]. In this compound, the six-membered esteric ring of the $[OCH_2C(CH_3)_2CH_2O]P(O)$ part illustrates a nearly-chair conformation with Cremer and Pople puckering parameters [49] Q = 0.5632 (15) Å, θ = 175.03 (14)° and φ = 323.2 (17)° for the P1/O2/C8/C7/C6/O3 ring. In this esteric ring, the P═O bond is located in a position intermediate between equatorial and axial (with angles $O_P{=}_O{-}P{-}O_{estric}$ = 113.68 (7)° and 114.39 (7)°, $O_P{=}_O{-}P{-}N$ = 115.15 (8)° and $O_{estric}{-}P{-}N$ = 105.43 (9)° and 104.30 (8)°). Such an intermediate position of the P═O bond has also been observed for similar amidophosphoric acid esters with a tertiary mine [27].

The molecular packing of the structure **1** consists of N–H···Cl hydrogen-type bonds (Table 2) displaying a 1D linear arrangement formed along the [010] direction building $R_2^2(12)$ motif rings (Fig. 3). Moreover, a comparison of the complex **1** with its free ligand [28] shows that in both structures the molecular assembly is as a linear arrangement formed by the N–H···O/Cl interactions, where the N–H···O═P hydrogen bonds in free ligand are replaced with N–H···Cl in the complex **1**. Indeed, with the coordination of free ligand to tin metal and the involvement of the phosphoryl group in the Sn···O═P interaction in the complex, the chlorine atom of $Sn(CH_3)_2Cl_2$ segment in **1** instead of the favoured acceptor P═O unit in free ligand acts as a hydrogen bond acceptor.

In the case of **2**, the phosphoryl group in this structure acts as a strong hydrogen-bond acceptor, but strong classical hydrogen-bond donors are not available so that it interacts with the available weaker hydrogen-bonding donors which are part of the methyl (intermolecular) and methylene (intramolecular) groups or of the aromatic ring. Thus, the structure **2** can be brought up as a model of one-acceptor system to form normal hydrogen bond interaction, while the structure **1** is a one-acceptor-one-donor system, where one-acceptor and one-donor refer to the P═O and N─H groups, respectively.

### 3.3. Hirshfeld surface (HS) analysis

A Hirshfeld surface analysis is carried out in order to evaluate the intermolecular interactions presented within the crystal structures of the compounds **1** and **2**. Figs. 4 and 5 show Hirshfeld surfaces mapped over the $d_{norm}$ property and the shape index and the associated full 2D fingerprint (FP) plots. The decomposed FPs are shown in Figs. S8 and S9. Table 3 provides the intermolecular

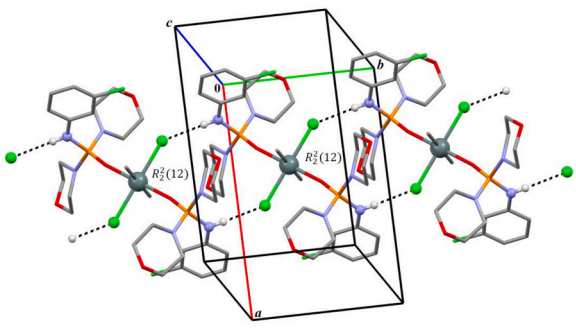


**Fig. 3.** Partial view of the one-dimensional linear molecular assembly formed *via* N–H···Cl hydrogen bond interactions (black dash lines) along the *b* axis in the crystal structure of **1** building the $R_2^2(12)$ motif rings. H atoms not involved in hydrogen bond interactions have been omitted for clarity and the metal tin atoms along with the contact atoms Cl, N and H have been shown as "ball and stick".

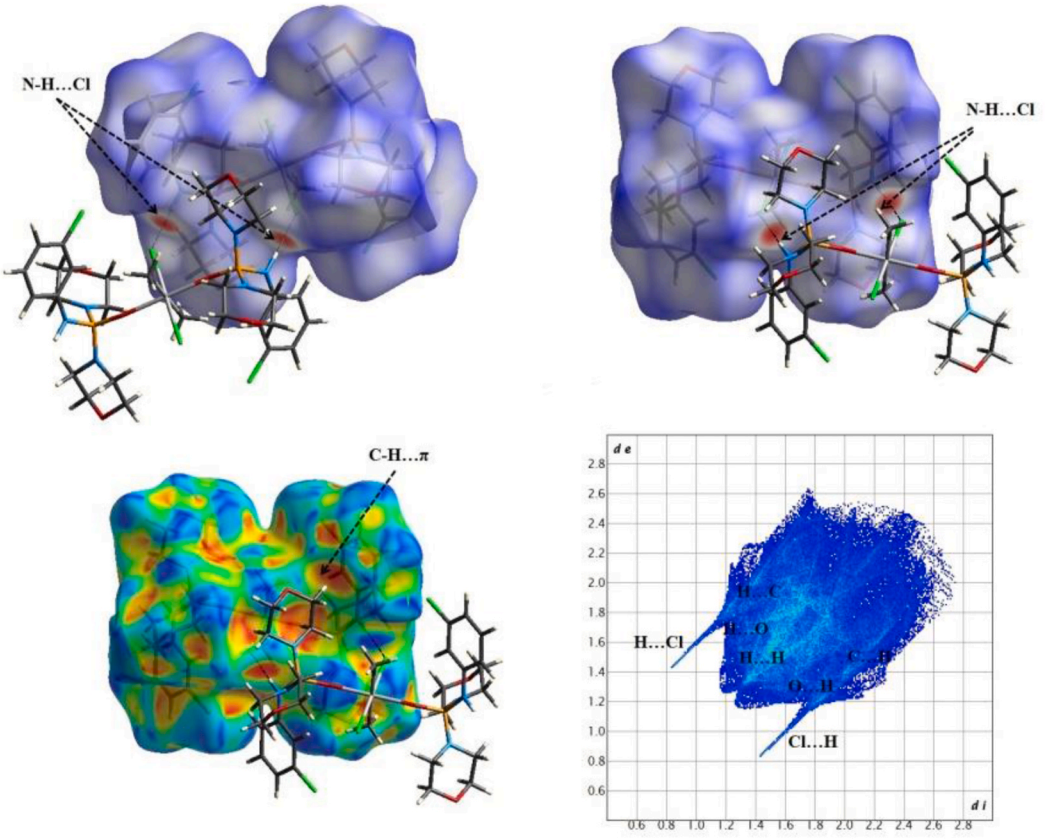


**Fig. 4.** Views of the Hirshfeld surface maps for the compound **1** calculated based on the $d_{norm}$ (up), in two orientations, and shape index (down left) properties. The corresponding full fingerprint plot (down right) labeling features related to the main intermolecular contacts is shown at the right side of the figure.

contacts contributions relative to the HS areas and the calculated enrichment ratios (*E*).

For the compound **1**, the chlorine atom of the $Sn(CH_3)_2Cl_2$ segment and the hydrogen atom of the NH unit as the favorable acceptor and donor sites, respectively, involved in N–H···Cl hydrogen bond interaction (N8–H8···Cl24, Table 2) are identified as the obvious red spots on the $d_{norm}$ HS. In the case of the compound **2**, some little red areas are seen on the surface which are related to non-classical intermolecular C–H···O═P (C16–H161···O4 between the aromatic CH group with the phosphoryl group and C10–H102···O4 between the methyl $CH_3$ group of the steric ring with the phosphoryl group, Table 2). Moreover, some π-effect interactions of type C–H … π (C20–H202 … π between the methylene $CH_2$ group with the centroid of aromatic ring in **1** and C18–H182 … π between the methyl $CH_3$ group of the N–$CH_3$ unit with the centroid of aromatic ring in **2**, Table 2) are indicated as "red π-holes" pattern on the shape index surfaces (Figs. 4 and 5).

Based on the information from the FPs, the H···H interactions can be calculated for both two structures to cover the largest region of the FPs concentrated around the diagonal plot: 55.7% for **1** and 67.9% for **2**. Some of these H···H contacts with values $d_i + d_e \approx 2.4$ Å for **1** and 2.2 Å for **2**, *i.e.* less than 2 × the van der Waals radius of hydrogen atom appear on the diagonal plot. For **1**, two sharp spikes on the FP with a lowest value of $d_i + d_e \approx 2.2$ Å are seen for H···Cl/Cl···H contacts indicative of relatively strong hydrogen bond interactions N–H···Cl. Such contacts are at values less than the sum of the van der Waals radii of the chlorine and hydrogen atoms (≈2.85 Å). In the case of **2**, no such sharp spikes are observed on the FP, but there are two very short spikes related to H···O/O···H contacts (19.2%) with a lowest value of $d_i + d_e \approx 2.5$ Å which is close to the sum of the van der Waals radii of the oxygen and hydrogen atoms (≈2.6 Å). For **1**, these H···O/O···H contacts (13.2%) cover the regions of the upper-left and down-right of the diagonal plot. Other considerable contacts are the H···C/C···H ones which contribute 7.9% and 12.2% of the total HS, respectively for **1** and **2**. Furthermore, in **1**, a characteristic feature on the FP is found corresponding to the Cl···C/C···Cl contacts comprising minor proportions 1.0% of the HS.

The results of the enrichment ratio calculations given in Table 3 show that H···Cl/Cl···H (for **1**) and H···O/O···H (for **2**) contacts covering the hydrogen bond interactions N–H···Cl and C–H···O═P, respectively, appearing as red spots on the HS and with enrichment ratios higher than unity are favoured. However, the enrichment ratio of the H···O/O···H contacts in **1** is calculated to be 1.31 and consequently is also favoured. The H···C/C···H contacts for both structures **1** and **2** and the C···Cl/Cl···C contacts for **1**, with enrichment ratios higher than unity (Table 3) turn out to be favoured in the crystal packing of the studied compounds. The H···H contacts in the structures of both **1** and **2** have the highest contribution to the total HS and the values of the surface contact $S_H$ and the

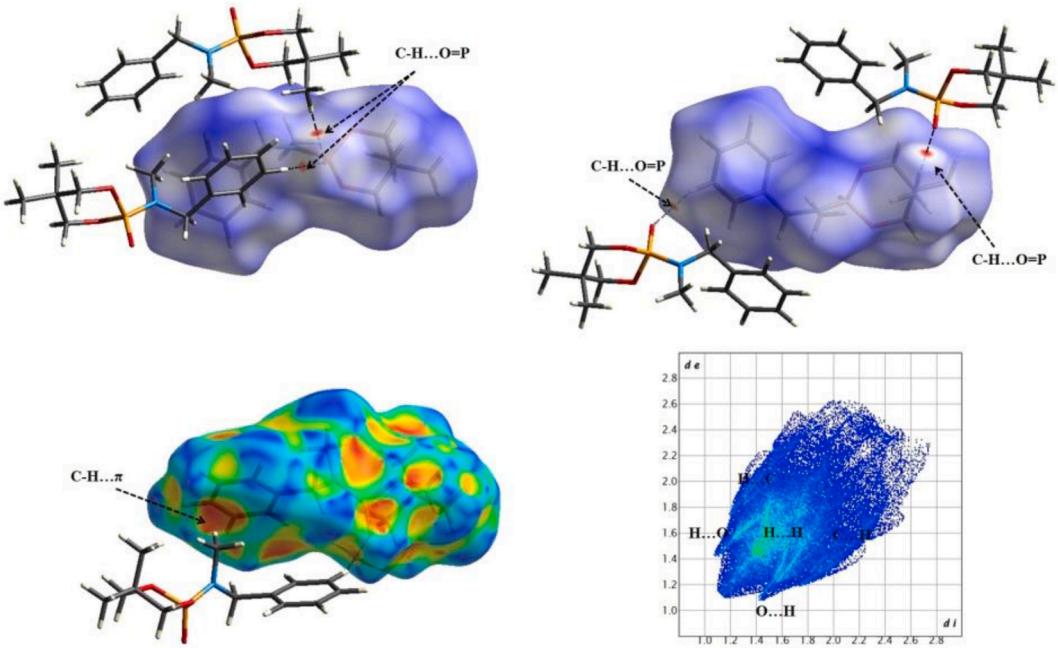


**Fig. 5.** Views of the Hirshfeld surface maps for the compound **2** calculated based on the $d_{norm}$ (up), in two orientations, and shape index (down left) properties. The corresponding full fingerprint plot (down right) is shown at the right side of the figure.

random contact $R_{HH}$ but are impoverished ($E_{HH} < 1$).

### *3.4. Molecular docking study*

In the docking simulation process the inhibitory potential of the studied compounds against the target protein viruses is evaluated by selecting the best pose of the studied compound towards the receptor with the highest affinity among the different poses. Figs. 6 and 7 display the results of the docking simulation on the compounds **1** and **2** against 6LU7 and 4QWO, respectively.

In the case of the target protein 6LU7 of SARS-CoV-2, the best affinity scores calculated in AutoDock as a binding energy are −6.05 and −6.29 kcal/mol for the compounds **1** and **2**, respectively. The obtained energies are negative which may confirm the interaction of **1** and **2** with 6LU7 as a destructive effect on the activity of this protein. On the other hand, a comparison of these energy values with those of the coronavirus drugs such as Remdesivir (−7.2 kcal/mol), Chloroquine (−5.4 kcal/mol) and Hydroxychloroquine (−5.6 kcal/mol) [53] reveals that the compounds **1** and **2** can be proposed as potential inhibitors of $M^{Pro}$ of SARS-CoV-2. It can be interesting that based on the docking simulation on free ligand of the complex **1** against 6LU7 [28], the binding energy was calculated about −6.12 kcal/mol. As it is seen, this value for free ligand is slightly higher compared to the calculated binding energy for **1**. This outcome can be attributed to the presence of the uncoordinated P═O unit in free ligand that it as a favoured hydrogen bond acceptor unit can be interacted with different sections of a biological target, while in the complex **1**, the P═O group is involved in interaction with the tin metal center as Sn···O═P.

The conceivable interactions between the studied structures **1** and **2** and the biological target 6LU7 are shown in Fig. 6. The aromatic ring of the 3-chloroaniline substituent of the phosphoric triamide ligand in complex **1** interacts with the amino acid residues of MET49 and SER46, whereas, the aliphatic morpholine rings of the ligand interact with the ASN142 and GLN189. In the case of **2**, the interactions are found between the aromatic ring of the *N*-methylbenzylamido substituent with the amino acid residues of MET49 and HIS41. Some interactions are present between the esteric ring $P[OCH_2C(CH_3)_2CH_2O]$ with the HIS163 and CYS145 residues. Other considerable contacts are between GLN189 with the $CH_2$ group of the benzylamid substituent and between the oxygen atom of the phosphoryl group with GLU166.

Moreover, based on the obtained results of the conceivable interactions discussed above, the larger binding energy calculated for the amidophosphoric acid ester **2** compared with the organotin(IV)-phosphoric triamide complex **1** can be attributed to the involvement of the P═O group as a strong hydrogen bond acceptor unit in interaction with the amino acid residues for **2**. Such interactions by helping the phosphoryl group are not possible for the complex **1**, where the P═O group has been coordinated to the tin metal center as Sn···O═P. Furthermore, recently we have carried out the molecular docking study on the different families of phosphoramides (phosphoric triamides [17,28], amidophosphoric acid esters [27] and some of phosphoric triamide $Co^{2+}$ and $Cu^{2+}$ complexes [19]) to evaluate their inhibitory activity against $M^{Pro}$ of SARS-CoV-2. The results of these studies show the negative binding energies in the range −4.7 to −6.9 kcal/mol for the ligand–protein interactions suggested as anti-coronavirus. A comparison of the obtained docking data in here with the mentioned docking simulations illustrates the organotin(IV)-phosphoric triamide complex

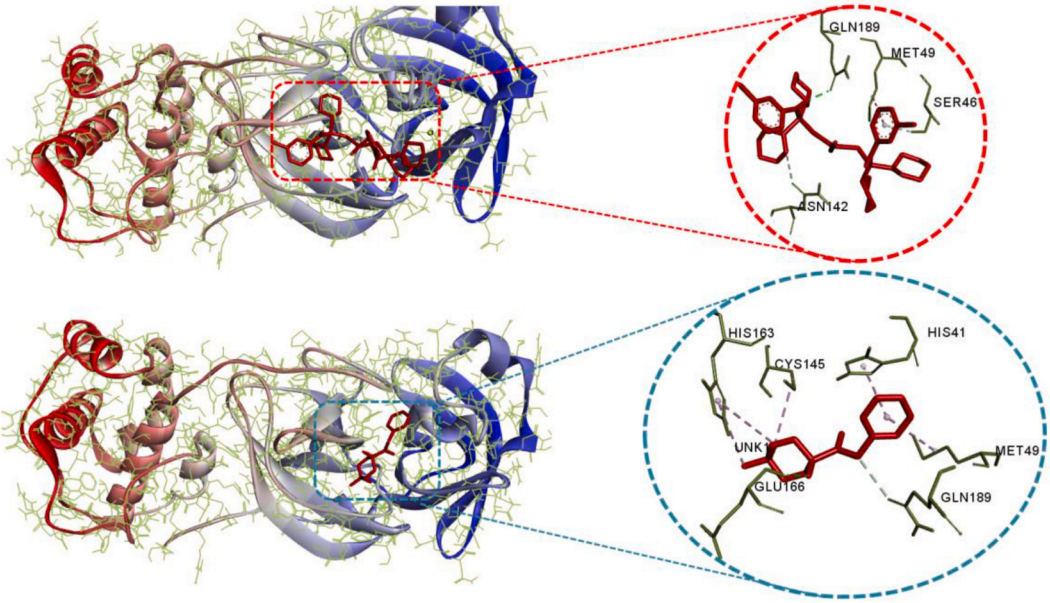


**Fig. 6.** Left: Visual description of the 3D compounds **1** (up) and **2** (down) in the best position relative to 6LU7 showing the highest negative binding affinity; Right: The 2D representation maps of **1** and **2** with amino acid sites inside of the active pocket of 6LU7.

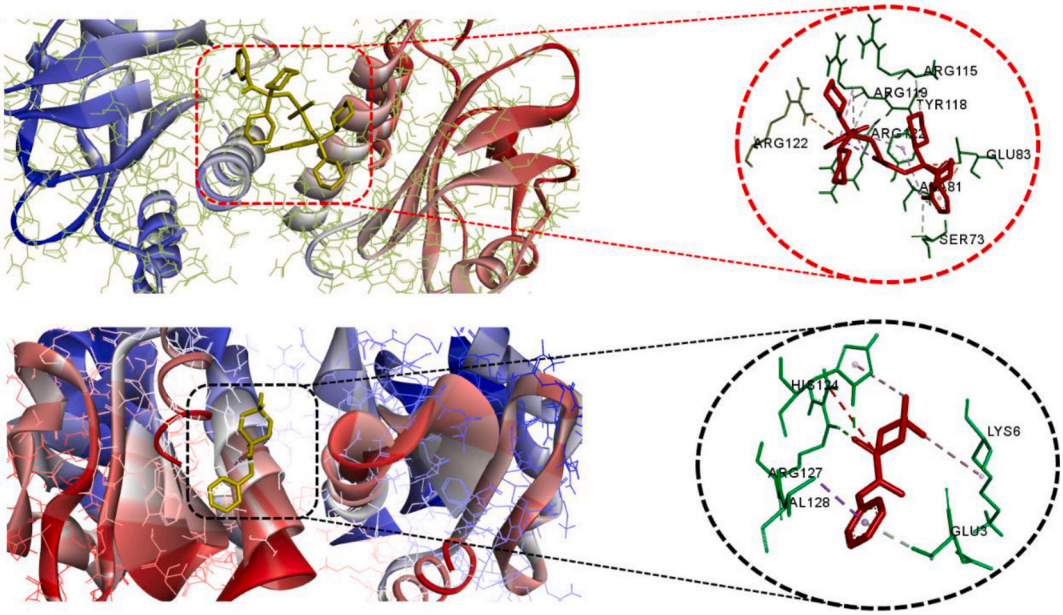


**Fig. 7.** Left: Visual description of the 3D compounds **1** (up) and **2** (down) in the best position relative to 4QWO showing the highest negative binding affinity; Right: The 2D representation maps of **1** and **2** with amino acid sites inside of the active pocket of 4QWO.

(**1**) and the amidophosphoric acid ester (**2**) also show the negative binding energies in the quoted range; so such phosphoramide compounds can be suggested as suitable candidates to inhibit the coronavirus.

In the case of the target protein 4QWO of Monkeypox, affinity score values of −6.58 and −6.53 kcal/mol are computed for the compounds **1** and **2**, respectively. These negative values point to a possible disruption of the protein activity suggesting the compounds **1** and **2** could be potential inhibitors of Monkeypox. However, the binding energy affinity scores between 4QWO and Monkeypox drugs such as Tecovirimat (−9.6 kcal/mol for 4QWO) and Brincidofovir (−9.8 kcal/mol) [54] are slightly more negative.

As is seen in Fig. 7, the major interactions between the structure **1** and the biological target 4QWO are between the aromatic rings of **1** with the amino acid residues of ARG122, ARG119 and GLU83. Other interactions are between the chlorine atom of the aromatic rings

with the SER73, ALA81 and TYR188 and between the aliphatic morpholine rings with the ARG155. For **2**, some interactions are present between the aromatic ring of the *N*-methylbenzylamido substituent with GLU3 and VAL128, and between the phosphoryl group with the ARG127. Moreover, the amino acid residues of HIS124 and LYS6 interact with the esteric ring P[$OCH_2C(CH_3)_2CH_2O$] of **2**. As it is seen, both compounds **1** and **2** bear the aromatic rings which play a significant role in interaction with the biological target. This structural similarity might justify the almost same binding energies in the case of the biological target 4QWO for **1** and **2**.

## 4. Conclusions

The molecular and crystal structures of two new phosphoramide compounds, i.e. a novel organotin(IV)-phosphoramide complex (**1**) and a new amidophosphoric acid ester (**2**), were investigated by a structural and Hirshfeld surface analysis and by a molecular docking study. The X-ray crystallographic data elucidate that the tin(IV) center of the complex **1** is six-coordinate with a distorted octahedral geometry at a Sn(*trans*-$Cl_2$)(*trans*-$(CH_3)_2$)(*trans*-$(PO)_2$) environment (PO = phosphoric triamide ligand). The supramolecular assembly of **1** is a 1D linear arrangement along the *b* axis formed by N–H···Cl hydrogen bonds, whereas for **2**, the crystal packing is devoid of any classical hydrogen bond interaction. The Hirshfeld surface analysis illustrates that the most favoured intermolecular interactions are of the type H···Cl/Cl···H (for **1**) and H···O/O···H (for **1** and **2**) covering the hydrogen bond interactions N–H···Cl and C–H···O═P, respectively. The inhibitory role of the compounds **1** and **2** on the SARS-CoV-2 (6LU7) and the Monkeypox (4QWO) proteins was evaluated by molecular docking simulation which suggests a suitable inhibitory potential, especially in the case of 6LU7 with a binding energy score comparable with reported drugs against the coronavirus.

## Data availability

No data was used for the research described in the article.

## Declaration of competing interest

The authors declare that they have no known competing financial interests or personal relationships that could have appeared to influence the work reported in this paper.

## Acknowledgements

Support of this investigation by Semnan University is gratefully acknowledged.

## Appendix A. Supplementary data

Supplementary data to this article can be found online at https://doi.org/10.1016/j.heliyon.2023.e17358.

## References

[1] A.A. Elfiky, Ribavirin, remdesivir, Sofosbuvir, galidesivir, and Tenofovir against SARS-CoV-2 RNA dependent RNA polymerase (RdRp): a molecular docking study, Life Sci. 258 (2020), 118350, https://doi.org/10.1016/j.lfs.2020.117592.
[2] A. Gasmi, M. Peana, S. Noor, R. Lysiuk, A. Menzel, A. Gasmi Benahmed, G. Bjørklund, Chloroquine and hydroxychloroquine in the treatment of COVID-19: the never-ending story, Appl. Microbiol. Biotechnol. 105 (2021) 1333–1343, https://doi.org/10.1007/s00253-021-11094-4.
[3] H. Adler, S. Gould, P. Hine, L.B. Snell, W. Wong, C.F. Houlihan, J.C. Osborne, T. Rampling, M.B. Beadsworth, C.J. Duncan, J. Dunning, T.E. Fletcher, E. R. Hunter, M. Jacobs, S.H. Khoo, W. Newsholme, D. Porter, R.J. Porter, L. Ratcliffe, M.L. Schmid, M.G. Semple, A.J. Tunbridge, T. Wingfield, N.M. Price, Clinical features and management of human monkeypox: a retrospective observational study in the UK, Lancet Infect. Dis. 22 (2022) 1153–1162, https://doi.org/10.1016/S1473-3099(22)00228-6.
[4] C. Huang, Y. Wang, X. Li, L. Ren, J. Zhao, Y. Hu, L. Zhang, G. Fan, J. Xu, X. Gu, Z. Cheng, T. Yu, J. Xia, Y. Wei, W. Wu, X. Xie, W. Yin, H. Li, M. Liu, Y. Xiao, H. Gao, L. Guo, J. Xie, G. Wang, R. Jiang, Z. Gao, Q. Jin, J. Wang, B. Cao, Clinical features of patients infected with 2019 novel coronavirus in Wuhan, China, Lancet 395 (2020) 497–506, https://doi.org/10.1016/S0140-6736(20)30183-5.
[5] A. Lassoued, A.B. Saad, H. Lassoued, R. Ketata, O. Boubaker, Dataset on the COVID-19 Pandemic Situation in Tunisia with Application to SIR Model, 2020, https://doi.org/10.1101/2020.04.23.20076802 medRxiv, PPR155789.
[6] M. Pourayoubi, S. Shoghpour Bayraq, A. Tarahhomi, M. Nečas, K. Fejfarová, M. Dušek, Hirshfeld surface analysis of new organotin (IV)-phosphoramide complexes, J. Organomet. Chem. 751 (2014) 508–518, https://doi.org/10.1016/j.jorganchem.2013.10.009.
[7] A. Tarahhomi, A. van der Lee, A new six-coordinate organotin (IV) complex of OP[$NC_5H_{10}$]$_3$: a comparison with an analogous five-coordinate complex by means of X-ray crystallography, Hirshfeld surface analysis and DFT calculations, J. Coord. Chem. 71 (2018) 1575–1592, https://doi.org/10.1080/00958972.2018.1461847.
[8] B. Bakhshipour, A. Tarahhomi, A. van der Lee, Synthesis and structural study of five new phosphoric triamides: interplay between classical and non-classical intermolecular interactions, Z. für Kristallogr. - Cryst. Mater. 236 (2021) 301–312, https://doi.org/10.1515/zkri-2021-2050.
[9] T. Venkatachalam, P. Samuel, S. Qazi, F. Uckun, Effect of change in nucleoside structure on the activation and antiviral activity of phosphoramidate derivatives, Bioorg. Med. Chem. 13 (2005) 5408–5423, https://doi.org/10.1016/j.bmc.2005.04.083.
[10] W. Wu, R.F. Borch, Synthesis and biological activity of *N*-2,3-dihydroxypropyl-*N*-4-chlorobutyl nucleoside phosphoramidate prodrugs, Mol. Pharm. 3 (2006) 451–456, https://doi.org/10.1021/mp060006g.
[11] C. Congiatu, A. Brancale, M.D. Mason, W.G. Jiang, C. McGuigan, Novel potential anticancer naphthyl phosphoramidates of BVdU: separation of diastereoisomers and assignment of the absolute configuration of the phosphorus center, J. Med. Chem. 49 (2006) 452–455, https://doi.org/10.1021/jm0509896.

[12] N. Dorosti, B. Delfan, M. Khodadadi, Ultrasonic-assisted synthesis and biological evaluation of a nano-rod diorganotin phosphonic diamide: precursor for the fabrication of $SnP_2O_7$ nano-structure, Appl. Organomet. Chem. 31 (2017) e3875, https://doi.org/10.1002/aoc.3875.

[13] P. Krishna, D. Srinivasulu, V.S. Kotakadi, Synthesis, characterization, and antibacterial activity of new linezolid-based phosphoramidate derivatives, Phosphorus, Sulfur, Silicon Relat. Elem. 189 (2014) 1557–1563, https://doi.org/10.1080/10426507.2014.902835.

[14] M.R. Sivala, V. Chintha, K.M. Potla, S. Chinnam, N.R. Chamarthi, In silico docking studies and synthesis of new phosphoramidate derivatives of 6-fluoro-3-(piperidin-4-yl) benzo[*d*]isoxazole as potential antimicrobial agents, J. Recept. Signal Transduct. Res. 40 (2020) 486–492, https://doi.org/10.1080/10799893.2020.1752719.

[15] K. Gholivand, M.H.H. Koupaei, F. Mohammadpanah, R. Roohzadeh, N. Fallah, M. Pooyan, M. Satari, F. Pirastehfar, A novel phospho triazine compound serving as an anticancer and antibacterial agent: an experimental-computational investigation, J. Mol. Struct. 1263 (2022), 133024, https://doi.org/10.1016/j.molstruc.2022.133024.

[16] K. Gholivand, L. Asadi, A.A.E. Valmoozi, M. Hodaii, M. Sharifi, H.M. Kashani, H.R. Mahzouni, M. Ghadamyari, A.A. Kalate, E. Davari, Phosphorhydrazide inhibitors: toxicological profile and antimicrobial evaluation assay, molecular modeling and QSAR study, RSC Adv. 6 (2016) 24175–24189, https://doi.org/10.1039/C5RA24209F.

[17] E. Gholamnezhad, A. Tarahhomi, A. van der Lee, Energy frameworks and Hirshfeld surface analysis of supramolecular features in three new phosphoric triamides: tuning the intermolecular interactions via the substituent effect, J. Mol. Struct. 1259 (2022), 132742, https://doi.org/10.1016/j.molstruc.2022.132742.

[18] K. Gholivand, A. Barzegari, F. Mohammadpanah, R. Yaghoubi, R. Roohzadeh, A.A.E. Valmoozi, Synthesis, characterized, QSAR studies and molecular docking of some phosphonates as COVID-19 inhibitors, Polyhedron 221 (2022), 115824, https://doi.org/10.1016/j.poly.2022.115824.

[19] M. Najarianzadeh, A. Tarahhomi, S. Pishgo, A. van der Lee, Experimental and theoretical study of novel amino-functionalized P(V) coordination compounds suggested as inhibitor of $M^{Pro}$ of SARS-COV-2 by molecular docking study, Appl. Organomet. Chem. 36 (2022), e6636, https://doi.org/10.1002/aoc.6636.

[20] A.J. Wiemer, Metabolic efficacy of phosphate prodrugs and the remdesivir paradigm, ACS Pharm. Trans. Sci. 3 (2020) 613–626, https://doi.org/10.1021/acsptsci.0c00076.

[21] M.A. Abu-Zaied, S.F. Hammad, F.T. Halaweish, G.H. Elgemeie, Sofosbuvir thio-analogues: synthesis and antiviral evaluation of the first novel pyridine-and pyrimidine-based thioglycoside phosphoramidates, ACS Omega 5 (2020) 14645–14655, https://doi.org/10.1021/acsomega.0c01364.

[22] A.A. Al-Karmalawy, M.A. Dahab, A.M. Metwaly, S.S. Elhady, E.B. Elkaeed, I.H. Eissa, K.M. Darwish, Molecular docking and dynamics simulation revealed the potential inhibitory activity of ACEIs against SARS-CoV-2 targeting the *h*ACE2 receptor, Front. Chem. 9 (2021), 661230, https://doi.org/10.3389/fchem.2021.661230.

[23] G. Sliwoski, S. Kothiwale, J. Meiler, E.W. Lowe, Computational methods in drug discovery, Pharmacol. Rev. 66 (2014) 334–395, https://doi.org/10.1124/pr.112.007336.

[24] S. Kansız, A. Tolan, M. Azam, N. Dege, M. Alam, Y. Sert, S.I. Al-Resayes, H. İçbudak, Acesulfame based Co(II) complex: synthesis, structural investigations, solvatochromism, Hirshfeld surface analysis and molecular docking studies, Polyhedron 218 (2022), 115762, https://doi.org/10.1016/j.poly.2022.115762.

[25] Ö. Tamer, H. Mahmoody, K.F. Feyzioğlu, O. Kılınç, D. Avci, O. Orun, N. Dege, Y. Atalay, Synthesis of the first mixed ligand Mn(II) and Cd(II) complexes of 4-methoxy-pyridine-2-carboxylic acid, molecular docking studies and investigation of their anti-tumor effects in vitro, Appl. Organomet. Chem. 34 (2020) e5416, https://doi.org/10.1002/aoc.5416.

[26] K. Gholivand, F. Mohammadpanah, M. Pooyan, R. Roohzadeh, Evaluating anti-coronavirus activity of some phosphoramides and their influencing inhibitory factors using molecular docking, DFT, QSAR, and NCI-RDG studies, J. Mol. Struct. 1248 (2022), 131481, https://doi.org/10.1016/j.molstruc.2021.131481.

[27] N. Heidari, A. Tarahhomi, A. van der Lee, Structural and molecular packing study of three new amidophosphoric acid esters and assessment of their inhibiting activity against SARS-CoV-2 by molecular docking, ChemSelect 7 (2022), e202201504, https://doi.org/10.1002/slct.202201504.

[28] M. Najarianzadeh, A. Tarahhomi, A. van der Lee, Different phosphoric triamide $[HN]_{3-n}P(O)[N]_n$ (n= 1, 2) skeletons lead to identical non-covalent interactions assemblies: X-ray crystallography investigation, Hirshfeld surface analysis and molecular docking study against SARS-CoV-2, Inorg. Chim. Acta. 543 (2022), 121190, https://doi.org/10.1016/j.ica.2022.121190.

[29] C.R. Groom, I.J. Bruno, M.P. Lightfoot, S.C. Ward, The Cambridge structural database, Acta Crystallogr. B 72 (2016) 171–179, https://doi.org/10.1107/S2052520616003954.

[30] Agilent, *CrysAlis PRO* Version 1.171.38.43c, Agilent Technologies, Yarnto Oxfordshire, England, 2011.

[31] A. van der Lee, Charge flipping for routine structure solution, J. Appl. Crystallogr. 46 (2013) 1306–1315, https://doi.org/10.1107/S0021889813020049.

[32] L. Palatinus, G. Chapuis, *SUPERFLIP*–a computer program for the solution of crystal structures by charge flipping in arbitrary dimensions, J. Appl. Crystallogr. 40 (2007) 786–790, https://doi.org/10.1107/S0021889807029238.

[33] P.W. Betteridge, J.R. Carruthers, R.I. Cooper, K. Prout, D.J. Watkin, *CRYSTALS* version 12: software for guided crystal structure analysis, J. Appl. Crystallogr. 36 (2003) 1487, https://doi.org/10.1107/S0021889803021800.

[34] A.L. Spek, Structure validation in chemical crystallography, Acta Crystallogr. D 65 (2009) 148–155, https://doi.org/10.1107/S090744490804362X.

[35] C.F. Macrae, I.J. Bruno, J.A. Chisholm, P.R. Edgington, P. McCabe, E. Pidcock, L. Rodriguez-Monge, R. Taylor, J. Streek, P.A. Wood, Mercury CSD 2.0–new features for the visualization and investigation of crystal structures, J. Appl. Crystallogr. 41 (2008) 466–470, https://doi.org/10.1107/S0021889807067908.

[36] I.J. Bruno, J.C. Cole, M. Kessler, J. Luo, W.S. Motherwell, L.H. Purkis, B.R. Smith, R. Taylor, R.I. Cooper, S.E. Harris, A.G. Orpen, Retrieval of crystallographically-derived molecular geometry information, J. Chem. Inf. Comput. Sci. 44 (2004) 2133–2144, https://doi.org/10.1021/ci049780b.

[37] A. Tarahhomi, A. van der Lee, D.G. Dumitrescu, Evaluation of N–H···O hydrogen bond interactions in two new phosphoric triamides with a $P(O)[NHCH(CH_3)_2]_2$ segment by means of topological (AIM) calculations, Hirshfeld surface analysis and 3D energy framework approach, Z. für Kristallogr. - Cryst. Mater. 234 (2019) 401–413, https://doi.org/10.1515/zkri-2019-0005.

[38] S. Kansız, A.M. Qadir, N. Dege, S.H. Faizi, Two new copper (II) carboxylate complexes based on *N,N,N*′,*N*′-tetramethylethyleneamine: synthesis, crystal structures, spectral properties, dft studies and hirshfeld surface analysis, J. Mol. Struct. 1230 (2021), 129916, https://doi.org/10.1016/j.molstruc.2021.129916.

[39] S.D. Kanmazalp, M. Macit, N. Dege, Hirshfeld surface, crystal structure and spectroscopic characterization of (E)-4-(diethylamino)-2-((4-phenoxyphenylimino) methyl) phenol with DFT studies, J. Mol. Struct. 1179 (2019) 181–191, https://doi.org/10.1016/j.molstruc.2018.11.001.

[40] P.R. Spackman, M.J. Turner, J.J. McKinnon, S.K. Wolff, D.J. Grimwood, D. Jayatilaka, M.A. Spackman, CrystalExplorer: a program for Hirshfeld surface analysis, visualization and quantitative analysis of molecular crystals, J. Appl. Crystallogr. 54 (2021) 1006–1011, https://doi.org/10.1107/S1600576721002910.

[41] J.J. McKinnon, M.A. Spackman, A.S. Mitchell, Novel tools for visualizing and exploring intermolecular interactions in molecular crystals, Acta Crystallogr. B 60 (2004) 627–668, https://doi.org/10.1107/S0108768104020300.

[42] M.A. Spackman, J.J. McKinnon, Fingerprinting intermolecular interactions in molecular crystals, CrystEngComm 4 (2002) 378–392, https://doi.org/10.1039/B203191B.

[43] C. Jelsch, K. Ejsmont, L. Huder, The enrichment ratio of atomic contacts in crystals, an indicator derived from the Hirshfeld surface analysis, IUCrJ 1 (2014) 119–128, https://doi.org/10.1107/S2052252514003327.

[44] G.M. Morris, R. Huey, W. Lindstrom, M.F. Sanner, R.K. Belew, D.S. Goodsell, A.J. Olson, AutoDock4 and AutoDockTools4: automated docking with selective receptor flexibility, J. Comput. Chem. 30 (2009) 2785–2791, https://doi.org/10.1002/jcc.21256.

[45] BIOVIA, Discovery Studio Modeling Environment. Release, 4.5, Dassault Systemes, San Diego, CA, 2015.

[46] A. Tarahhomi, A. van der Lee, B. Ośmiałowski, A detailed theoretical and experimental study on the N-H, P=O and C=O stretching frequencies in two new phosphoric triamides and a statistical comparison with analogous structures, Polyhedron 158 (2019) 215–224, https://doi.org/10.1016/j.poly.2018.10.045.

[47] A.J. Metta-Magaña, M. Pourayoubi, K.H. Pannell, M.R. Chaijan, H. Eshtiagh-Hosseini, New organotin (IV)-phosphoramidate complexes: breaking of the P=O···H-N hydrogen bonds and its influence on the molecular packing, J. Mol. Struct. 1014 (2012) 38–46, https://doi.org/10.1016/j.molstruc.2012.01.024.

[48] A. Tarahhomi, M. Pourayoubi, A.L. Rheingold, J.A. Golen, Different orientations of C=O versus P=O in P(O)NHC(O) skeleton: the first study on an aliphatic diazaphosphorinane with a gauche orientation, Struct. Chem. 22 (2011) 201–210, https://doi.org/10.1007/s11224-010-9682-y.

[49] D. Cremer, J.A. Pople, General definition of ring puckering coordinates, J. Am. Chem. Soc. 97 (1975) 1354–1358, https://doi.org/10.1021/ja00839a011.
[50] M. Pourayoubi, A. Tarahhomi, J.A. Golen, A.L. Rheingold, The first coordination compounds of $OP[NC_4H_8O]_3$ phosphoric triamide ligand: structural study and Hirshfeld surface analysis of $Sn^{IV}$ and $Mn^{II}$ complexes, J. Coord. Chem. 70 (2017) 1285–1302, https://doi.org/10.1080/00958972.2017.1295139.
[51] M.S. Bozorgvar, A. Tarahhomi, A. van der Lee, Three new amidophosphoric acid esters with a $P(O)[OCH_2C(CH_3)_2CH_2O]$ segment: X-ray diffraction, DFT, AIM and Hirshfeld surface investigations of bi-and tri-furcated (three and four-center) hydrogen bond interactions, Z. für Kristallogr. - Cryst. Mater. 235 (2020) 69–84, https://doi.org/10.1515/zkri-2019-0050.
[52] M. Pourayoubi, A. Tarahhomi, A.L. Rheingold, J.A. Golen, Three new phosphoric triamides with a $[C(O)NH]P(O)[N(C)(C)]_2$ skeleton: a database analysis of C—N—C and P—N—C bond angles, Acta Crystallogr. C 70 (2014) 998–1002, https://doi.org/10.1107/S2053229614020488.
[53] R.R. Deshpande, A.P. Tiwari, N. Nyayanit, M. Modak, In silico molecular docking analysis for repurposing therapeutics against multiple proteins from SARS-CoV-2, Eur. J. Pharmacol. 886 (2020), 173430, https://doi.org/10.1016/j.ejphar.2020.173430.
[54] M.K. Dassanayake, T.-J. Khoo, C.H. Chong, P.D. Martino, Molecular docking and in-silico analysis of natural biomolecules against dengue, ebola, zika, SARS-CoV-2 variants of concern and monkeypox virus, Int. J. Mol. Sci. 23 (2022), 11131, https://doi.org/10.3390/ijms231911131.